The 193-nm Photodissociation of NCO

S. Gómez, H. M. Lambert, and P. L. Houston*

Department of Chemistry and Chemical Biology, Cornell University, Ithaca, New York 14853-1301

Received: February 8, 2001; In Final Form: April 13, 2001

The 193-nm photolysis of the NCO radical has been investigated. NCO was generated from the reaction of $CN + O_2$, where the CN was produced by 193-nm photolysis of C_2N_2 close to the nozzle of a pulsed jet. A second 193-nm photon dissociated the NCO radical during the same laser pulse. At this photon energy both the N−CO and the NC−O bonds may break. $N(^2D,^2P)$ and CO products have been detected using vacuum ultraviolet laser induced fluorescence. A direct measurement of the $N(^2D):N(^2P)$ branching ratio yielded an upper limit of 72 ± 18. The CO vibrational distribution was modeled with prior distributions for each of the contributing channels with coproducts $N(^4S,^2D,^2P)$. Combination of the results from the prior model and the direct measurement yielded a branching ratio of $N(^4S):N(^2D):N(^2P)$ of $(5.1 \pm 1.8):(93.6 \pm 4.8):(1.3 \pm 0.3)$. For the $N(^2D) + CO$ product channel, the average energy disposal into product relative translation (8%) and CO vibration (24%) was determined, leaving 68% of the available energy to appear as CO rotation. This observation suggests that the geometry of the dissociating state of NCO is likely bent.

Introduction

The NCO radical is a linear, open-shell molecule with 15 electrons and a ground-state electron configuration of $4\sigma^2 5\sigma^2 6\sigma^2 1\pi^4 7\sigma^2 2\pi^3$. Since its first optical detection some 40 years ago,[1] a great deal of effort has gone into unraveling the complex interactions that govern its spectrum.[2,3] One of the simpler, but nonetheless essential, features to come out of the ground-state analysis is the elongated equilibrium N−CO bond length (1.200 Å)[4] compared to free CN (1.1718 Å)[5] or HCN (1.1532 Å).[6] Accordingly, the C−N bond in NCO is considerably weaker than in other CN-containing species, by as much as 2 eV when compared to free CN, making NCO a highly reactive species. This shift to weaker C−N bond strength occurs in the oxidation of HCN and CN to NCO in the combustion of nitrogen-containing fuels.[7−9] Consequently, the key combustion reactions involving NCO are nitrogen atom abstraction reactions. Reactions with O and H atoms, for example, are important processes in the production of pollutant NO,[10] while reaction with NO is the basis of the RAPRENO$_x$ pollution reduction scheme in the treatment of combustion exhaust gases.[10,11]

The dissociation energetics of NCO are also characterized by a weak N−CO bond in that the lowest energy dissociation channels lead primarily to N and CO products. In this case, the bond strength is characterized by the nature of the excited state(s) participating in the dissociation. As determined by molecular orbital calculations and confirmed by experiment, the first excited state ($\tilde{A}^2\Sigma^+$) has a stronger N−CO bond than the ground state with a shortened bond length similar to that of free CN.[4,12,13] Several electronic configurations are predicted to be involved in the excitation to the second excited state ($\tilde{B}^2\Pi$),[14,15] one of which involves a transition ($3\pi^* \leftarrow 2\pi$) from a bonding molecular orbital to an antibonding molecular orbital[12] and results in a lengthened N−CO bond.[16] Dissociation from the $\tilde{B}$ state thus appears more likely than from the $\tilde{A}$ state. The four lowest product channels are listed below with the threshold wavelength at which the channel is energetically accessible:

$$NCO(\tilde{X}^2\Pi) + h\nu \rightarrow N(^4S) + CO(^1\Sigma^+) \quad \lambda_{thr} = 513 \text{ nm} \quad (1)$$

$$\rightarrow N(^2D) + CO(^1\Sigma^+) \quad \lambda_{thr} = 258 \text{ nm} \quad (2)$$

$$\rightarrow CN(X^2\Sigma^+) + O(^3P) \quad \lambda_{thr} = 215 \text{ nm} \quad (3)$$

$$\rightarrow N(^2P) + CO(^1\Sigma^+) \quad \lambda_{thr} = 205 \text{ nm} \quad (4)$$

Note that channel 1 is a spin-forbidden process correlating with a $^4\Sigma^-$ state, whereas the lower energy electronic states of NCO are all doublets. Channel 2 is the lowest energy spin-allowed dissociation.

The onset of dissociation was found experimentally to occur just below the $\tilde{B}$ state origin, which is between the thresholds indicated for channels 1 and 2. Wright et al.[17] probed the excited-state decay dynamics of many $\tilde{A}^2\Sigma^+$ and $\tilde{B}^2\Pi$ NCO vibronic levels over a wide spectral range using laser-induced fluorescence. Their measurements of radiative lifetimes as a function of excitation wavelength show a sudden decrease below 333 nm, indicating the onset of a nonradiative decay process.

Cyr et al. studied the photodissociation of NCO in the wavelength region between 305 and 234 nm.[18] Their results demonstrated that all vibronic levels of the $\tilde{B}^2\Pi$ state are predissociative, even below the onset to the spin-allowed channel 2. Near the origin, the $\tilde{B}^2\Pi$ state vibronic levels undergo spin-forbidden dissociation to $N(^4S) + CO(^1\Sigma^+)$. At vibrational levels above the threshold for the spin-allowed channel, however, dissociation to $N(^2D) + CO(^1\Sigma^+)$ dominates. Their velocity-based technique did not allow them to obtain detailed information about the internal energy distribution of the CO product.

Ab initio calculations of the electronic structure of NCO reveal a crossing between the $\tilde{A}^2\Sigma^+$ and $\tilde{B}^2\Pi$ potential energy surfaces occurring at an energy just above the $\tilde{B}^2\Pi$ state minimum.[19] Spin−orbit interaction between the $\tilde{A}^2\Sigma^+$ state and a repulsive $^4\Sigma^-$ state at an energy similar to that of the first crossing explains the onset of dissociation in the spin-forbidden channel. The exact mechanism of the spin-allowed dissociation

10.1021/jp010509w CCC: $20.00
Published on Web 06/09/2001

has not been determined, although it has been noted that for bent geometries the NCO $\tilde{B}$ state does correlate with the products of channel 2.[18]

The CN ($X^2\Sigma^+$, v, J) product state distribution was obtained in a study of the O + CN dissociation channel 3 at a photolysis wavelength of 193 nm.[20] The identity of the excited state(s) accessed at this wavelength is not known. A bimodal rotational distribution of the CN fragment was interpreted as evidence for the participation of two different excited electronic states of NCO in the dissociation. The authors proposed that the high-J CN fragments correlated with dissociation from a bent state, while the low-J CN resulted from dissociation from a linear state. Attempts to detect excited N atoms, either $N(^2D)$ or $N(^2P)$, using resonance fluorescence and chemical conversion techniques, were unsuccessful. On the basis of these results they concluded that the N + CO channel is a minor channel.

At higher energies more channels for the NCO dissociation open, leading to production of excited electronic states of the CN radical. Recently, Schoennenbeck et al.[21] detected the $CN(B^2\Sigma^+)$ radical from the VUV photolysis of NCO and determined the threshold wavelength for this channel. This was the first study of excited states above 6.5 eV and led to a tentative assignment of an n*s*-Rydberg series.

$$NCO(\tilde{X}^2\Pi) + h\nu \rightarrow CN(A^2\Pi) + O(^3P) \quad \lambda_{thr} = 180 \text{ nm} \quad (5)$$

$$\rightarrow CN(B^2\Sigma^+) + O(^3P) \quad \lambda_{thr} = 139 \text{ nm} \quad (6)$$

There is an additional dissociation channel in this energy region that has not yet been observed.

$$NCO(\tilde{X}^2\Pi) + h\nu \rightarrow NO(X^2\Pi) + C(^3P) \quad \lambda_{thr} = 178 \text{ nm} \quad (7)$$

Our long-range goal is to obtain the product state distributions after *tunable* ultraviolet photolysis of NCO. However, in attempting to measure CO generated from tunable ultraviolet photolysis, we found that the method of NCO generation produced strong background levels of CO. Before continuing with tunable photolysis, we decided to try to understand the source of this background. The experiments presented here generate the NCO radical early in an expansion of cyanogen, oxygen, and argon from the photoinitiated radical reaction scheme given by reactions 8 and 9, whereas the strong background appears to come from the concomitant production of CO by 10:

$$C_2N_2 + 193 \text{ nm} \rightarrow 2CN \quad (8)$$

$$CN + O_2 \rightarrow NCO + O \quad (9)$$

$$NCO + 193 \text{ nm} \rightarrow N + CO \quad (10)$$

As a result of the expansion, all products of the photolysis are rotationally and translationally cooled, but it is still possible to obtain the CO vibrational distribution, since this degree of freedom is inefficiently relaxed in the expansion.

The goals of our study of NCO photodissociation at 193 nm were thus 2-fold. First, we wanted to examine the product state energy distribution generated by the dissociation. This information will be useful in order to reduce any background signal when carrying out subsequent tunable ultraviolet photolysis of NCO. Second, we wanted to complement the 193-nm photodissociation studies previously conducted by Liu and Coombe.[20] Our investigation provides information concerning the product energy distribution to channels other than the CN + O channel they investigated. The work presented in this paper provides the first direct experimental determination of the distribution of energy in the $N^*(^2P,^2D)$ atoms and CO molecules generated from the 193-nm dissociation of NCO.

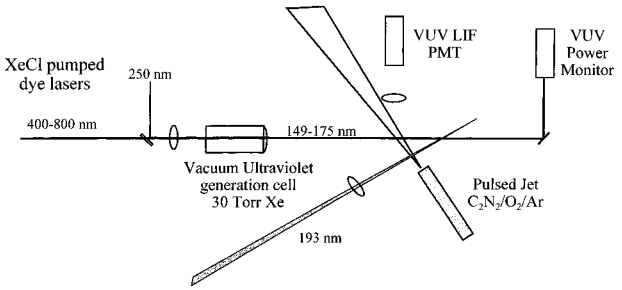

Figure 1. Schematic diagram showing the experimental arrangement of the molecular beam, the 193-nm photolysis laser, the VUV probe laser, the VUV LIF detection system, and the VUV laser monitor.

Experimental Setup

NCO radicals were generated in a molecular beam following laser initiation of the rapid CN + O_2 reaction. The gas mixture, 15% C_2N_2, 30% O_2, and balance Ar, was introduced to the vacuum chamber through a piezoelectric pulsed nozzle. Customarily, a backing pressure of 40 psig was used behind an orifice of 0.5 mm diameter. The valve was operated at 10 Hz with a pulse duration of 250 μs, resulting in a chamber pressure of 3×10^{-4} Torr. Typical background pressures were 8×10^{-7} Torr. The experimental apparatus has been described in detail previously.[22] As illustrated schematically in Figure 1, the CN reagent was prepared by the 193-nm laser dissociation of cyanogen, C_2N_2, at the tip of the jet. The typical pulse energy of the photolysis laser (Lambda Physik, COMPEX 201, ArF excimer) was 75 mJ, and the beam was focused to a vertical rectangle 2 mm $\times$ 5 mm. NCO was also photolyzed at 193 nm to give dissociation products. Both NCO production and photolysis occurred within the 20 ns laser pulse duration.

$N(^2D)$, $N(^2P)$, and CO were detected 50 nozzle diameters downstream using tunable vacuum ultraviolet laser induced fluorescence (VUV LIF). The N atoms were studied using the $3s\ ^2P_{3/2,1/2} \leftarrow 2s^22p^3\ ^2D_{3/2,5/2}$ transitions at 149.2625, 149.2820, and 149.4675 nm and the $3s\ ^2P_{3/2,1/2} \leftarrow 2s^22p^3\ ^2P_{3/2,1/2}$ transitions at 174.2729 and 174.5252 nm.[23] CO was monitored using the $A^1\Pi \leftarrow X^1\Sigma^+$ band system.

The VUV probe laser light was generated by four-wave mixing ($\omega_{VUV} = 2\omega_1 - \omega_2$) in Xe using an intermediate resonance with the $6p[1/2]_0$ state.[24] The output of a 308-nm XeCl excimer (Lambda Physik, LPX 205) was split and used to pump two dye lasers (Lambda Physik, FL 2002). The frequency-doubled output of the first dye laser, ω_1, was fixed to the two-photon resonance in Xe at 250.04 nm using a BBO crystal. The wavelength of the second dye laser, ω_2, was tuned from 440 to 800 nm with several dyes. A delay line was necessary to match both laser pulses in time and to obtain the optimum VUV power, which was typically about 10^9 photons. The delay line included a zero-order, 1/4-wave plate that rotated the ω_1 polarization to match that from ω_2, which was vertical in the laboratory frame. Before entering one arm of the chamber, both lasers were focused with a 4 in. focal length fused silica lens into the center of a 6 in. long cell containing 30 Torr of Xe. The resulting VUV radiation was recollimated with a 4 in. $f/1$ MgF_2 lens that acted both as the exit window of the Xe cell and entrance to the vacuum chamber. Laser energies were typically 0.25 and 2.5 mJ/pulse for ω_1 and ω_2, respectively.

With an etalon installed in ω_1, the VUV laser bandwidth (fwhm) was 0.21 cm^{-1}, as determined by scans over thermal CO(v=1) in a bulb experiment.

The VUV LIF signal from N* and CO products was detected by a solar-blind photomultiplier (SB PMT, EMR 542G-08-17) placed perpendicular to the plane formed by the molecular beam and the photolysis/probe lasers. An *f*/1 MgF_2 lens was employed for LIF signal collection. A MgF_2 193-nm high reflectance laser mirror was placed before the SB PMT in order to reduce the amount of scattered ArF laser light detected.

The NCO radical was probed via LIF using either the $\tilde{A}^2\Sigma^+ \leftarrow \tilde{X}^2\Pi$ at 440 nm or the $\tilde{B}^2\Pi \leftarrow \tilde{X}^2\Pi$ transitions at 315 nm. The $\tilde{A}-\tilde{X}$ system was probed using a XeCl excimer pumped dye laser system (Lambda Physik, LPX 205/ FL 2002). For the $\tilde{A}-\tilde{X}$ system, a Nd:YAG (Spectra Physics, GCR 270) pumped dye laser system (Lambda Physik, Scanmate 2E) was used. Frequency-doubling with a BBO crystal was needed for detection of LIF in the $\tilde{B}-\tilde{X}$ system. The CN radical was probed using a XeCl excimer pumped dye laser system (Lambda Physik, LPX 205/ FL 2002) tuned to the either the $B^2\Sigma^+ \leftarrow X^2\Sigma^+$ at 388 nm or the $B^2\Sigma^+ \leftarrow A^2\Pi$ transition at 480 nm. In these experiments, the solar-blind PMT was replaced by one sensitive to UV and visible light. A combination of cutoff filters was placed before the PMT in order to reduce the scattered laser light from the photolysis and probe lasers. A 390 nm interference filter was also used when employing the NCO $\tilde{B}$-$\tilde{X}$ LIF transition.

Power fluctuations in the CN/NCO probe laser were monitored after the chamber by sending a reflection of the laser beam into a cell filled with dye solution. The resulting fluorescence was detected using a fast photodiode (Thorlabs DET2000). The photodiode signal was processed by a boxcar and input to the data acquisition (DAQ) board/computer. The VUV laser energy was monitored at the opposite end of the vacuum chamber by using an additional solar-blind PMT (EMR 541G-08−17) placed at 90° upward in an elbow configuration. Reflections off a 45° window passed through a MgF_2 diffuser and a broad band VUV interference filter, placed before the SB PMT, to help reduce scattered ω_1 light. The output of this PMT was fed to a boxcar averager and input as one channel into the DAQ board/computer.

The photolysis laser energy was demonstrated to be stable during experiments, either by continuously monitoring a reflection off the entrance window to the chamber by means of a photodiode or by periodic measurements with a pyroelectric detector. The chamber pressure, on the other hand, fluctuated due to the mechanical characteristics of the pulsed valve. The pressure was monitored by using the analogue output of the ion gauge controller unit and collected on an additional channel on the DAQ board. The monitored signal fluctuations for pressure and photolysis/probe lasers were later used for normalization of the product LIF signal.

The experiment was computer-controlled by a program written in LabVIEW (National Instruments, version 5.0) that sent commands by means of GPIB interfaces to the digital delay generator, the laser computer/control units, the multichannel PC-DAQ I/O board, and the oscilloscope. The delay generator (Stanford Research Systems, DG535) set the main timing sequence between the nozzle opening and the trigger signals for firing the lasers. The laser wavelength was stepped using output pulses from the DAQ (National Instruments Lab PC+ DAQ board) I/O board sent to the laser controllers. Other inputs to the DAQ board were laser power monitor signals for both photolysis and probe lasers and the pressure monitor. The LIF signal was obtained by downloading the oscilloscope (LeCroy, 9450) trace, setting a gate on the feature of interest, and averaging for 10−20 shots.

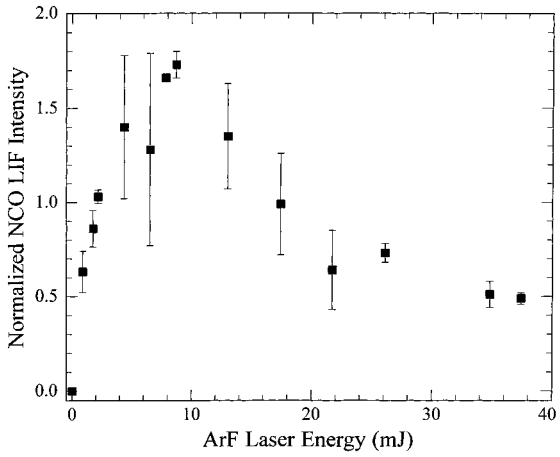

Figure 2. Photolysis of the 15% C_2N_2/30% O_2/55% Ar gas mixture at 193 nm yields an NCO LIF signal that strongly depends on the 193-nm laser pulse energy, consistent with processes 8−10.

Power dependencies of precursor and product molecule LIF signals were studied as a function of the photolysis laser energy. Several scans over a spectral feature of NCO, N*, or CO were conducted in which the LIF signal was monitored as a function of the photolysis laser energy. An iris or a set of fine wire mesh screens was used to attenuate the incident laser energy, which was measured using a calibrated pyroelectric detector. The dependence of the N(^{2}D) LIF signal on [C_2N_2] was also determined. Four mixtures with different cyanogen concentrations, 3%, 5%, 10%, and the usual 15%, were prepared for these measurements.

The gases used for this experiments, C_2N_2 (purity ≥ 98.5%, Matheson), O_2 (≥ 99.8%, Airgas), and Ar (99.999%, Spectra Gases), were used without further purification.

Results

Diagnostics. Several diagnostic experiments confirm that the interaction of the 193-nm laser with the molecular beam both produces and photolyzes NCO according to reactions 8−10. The power dependence studies summarized in Figure 2 clearly show that the NCO LIF signal initially rises rapidly with increasing 193-nm laser pulse energy. After this rise, a dramatic drop is observed at still fairly low (∼10−20 mJ/pulse) laser energies. The initial rise in NCO LIF at the lowest photolysis laser energies is evidence that the CN reagent, made by photolysis of C_2N_2 at 193 nm, is immediately reacting with the O_2 present in the expansion in order to produce NCO. The subsequent drop in NCO LIF at higher photolysis laser energies is a clear indication that the NCO absorbs a 193 nm photon and then dissociates into products. When the photolysis laser beam was focused less tightly, the plots of the NCO LIF signal vs 193-nm laser pulse energy showed higher signals for NCO that dropped less steeply with increasing pulse energy. Very mild focusing resulted in curves that did not drop but instead leveled off at higher laser pulse energies. Since cyanogen strongly absorbs at 193 nm, the plateau behavior is very likely due to saturation in the initial absorption step (reaction 8). From the fact that the NCO concentration measurements were made during the photolysis laser pulse, it is clear that this multiphoton process occurs on the time scale of a single photolysis laser pulse. The absence of the NCO signal when the probe laser preceded the photolysis laser illustrated that there was no NCO signal present from the previous gas and laser pulses.

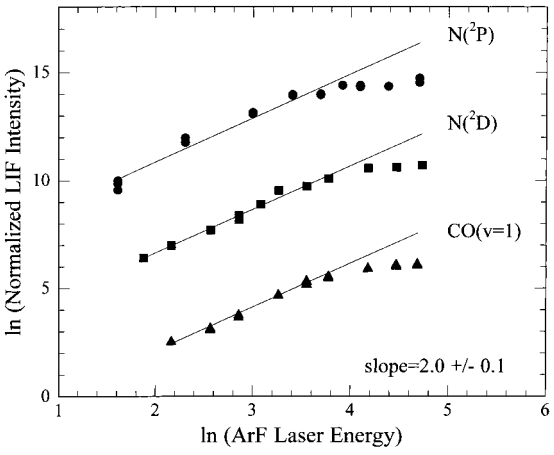

Figure 3. The N(^{2}D,^{2}P) and CO LIF signals depend quadratically on the 193-nm photolysis laser pulse energy, thus providing evidence for the two-photon process described by reactions 8−10. The solid lines were determined by least-squares fitting of the data. The plots have been displaced vertically.

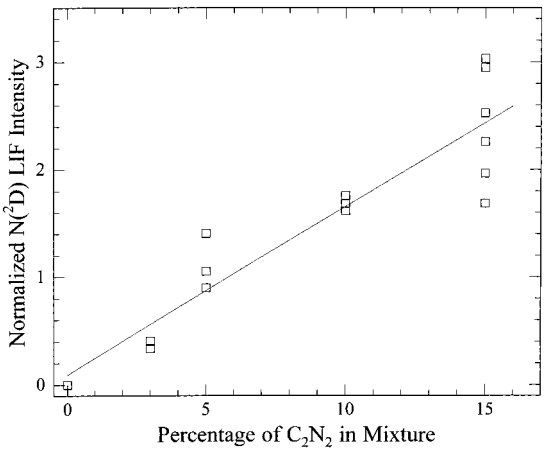

Figure 4. The N(^{2}D) LIF signal depends linearly on the percentage C_2N_2 in the beam, indicating that the excited nitrogen atoms are primary products of NCO photolysis.

The N(^{2}D), N(^{2}P), and CO concentrations depend quadratically on the 193-nm laser pulse energy at low pulse energy, as shown in Figure 3. This observation also agrees well with the proposition that a second 193-nm photon is absorbed by NCO to give these products. The slopes obtained by least-squares fitting to the linear part of the ln ln plot are 2.03 ± 0.12 for N(^{2}P), 2.02 ± 0.09 for N(^{2}D), 2.03 ± 0.11 for CO(v=1). The energy of the photolysis laser was maintained within the regions of quadratic behavior for detection of the N(^{2}D), N(^{2}P), and CO products for normalization purposes. However, it was demonstrated that the relative LIF intensities of the N* and CO products were the same both in the quadratic regime and at higher photolysis laser energies. This was taken as further evidence that the leveling off behavior with increasing 193-nm laser energies, observed for both NCO and product LIF signals, was due to saturation in the production of CN by photolysis of C_2N_2 (reaction 8), rather than saturation in the photolysis of NCO (reaction 10).

In the interaction region of the laser pulse and molecular beam, there are substantial concentrations of O and N atoms as well as the molecular species CO, CN, NCO, O_2, and C_2N_2. Studies of the N(^{2}D) LIF signal as a function of cyanogen concentration, [C_2N_2], were performed in order to discriminate against any other radical reactions that might be contributing to the species detected. Primary production of CO and N by photolysis of NCO at 193 nm predicts a linear dependence on the initial [C_2N_2], whereas CO and N production by secondary reactions of other species should have a quadratic dependence. Pressure dependence studies of the N(^{2}D) LIF signal on the percentage of C_2N_2 in the gas mixture, shown in Figure 4, exhibit a linear dependence, in keeping with the photolysis of NCO as the primary production source of CO and N.

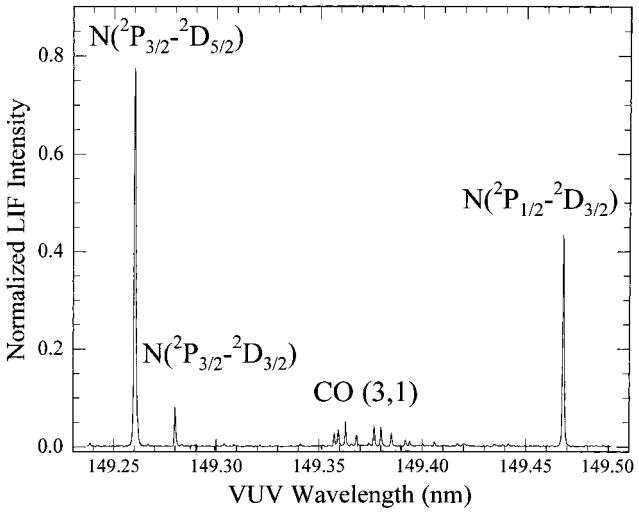

Figure 5. A portion of the product LIF spectrum containing the N(^{2}P$_J$←^{2}D$_J$) transitions and the CO($A^1\Pi$←$X^1\Sigma^+$) (3,1) band.

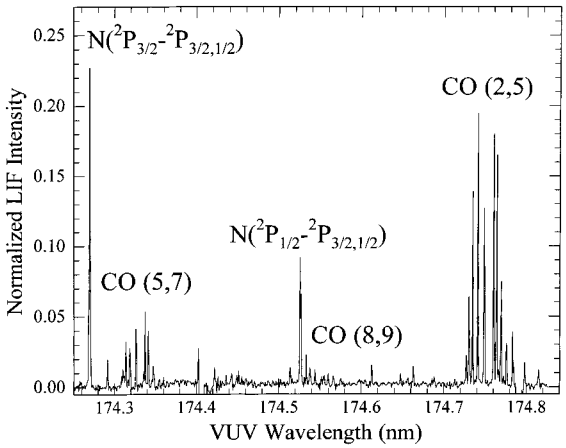

Figure 6. A portion of the product LIF spectrum containing the N(^{2}P$_J$←^{2}P$_J$) transitions and the CO (5,7), (8,9), and (2,5) bands.

The LIF spectra of CN, NCO, and CO show substantial rotational cooling since the reaction and dissociation occur early in the supersonic jet expansion. The rotationally resolved spectra of each vibronic band were simulated for both NCO and CO. The spectral intensities are well-characterized by a Boltzmann distribution with a rotational temperature of about 15 ± 5 K. Representative CO spectra in the regions of the N(^{2}D) and N(^{2}P) lines are shown in Figures 5 and 6, respectively.

The amount of rotational relaxation was studied by comparing the intensity of the LIF vibrational/rotational spectra probed at several distances downstream in the expansion. This was accomplished by moving the pulsed valve and 193-nm laser light closer to the center of the chamber and decreasing the delay time between the lasers to compensate for the shorter flight time. CO rotational distributions for vibrational levels v = 1 and 4 were observed to be significantly warmer when probed in regions closer to the photolysis laser and at times earlier in the gas pulse. The rotational temperatures were determined to be 15 K at a laser delay of 36 μs, 50 K at 8 μs, and 100 K at 4 μs.

Vibrational relaxation was also investigated. In the case of NCO, the LIF spectra showed not only rotational cooling but also extensive cooling of the bending vibrational motion. We thus worried that possible vibrational relaxation of the CO fragment during the expansion could affect its measured vibrational distribution. However, LIF spectra for both CO and CN showed no evidence of vibrational relaxation, even at long distances and delay times. In fact, the ratio of integrated band intensities for CO(v=1) and CO(v=4) remained unchanged to within the experimental uncertainties at delays of 4, 8, and 36 μs. This constant value demonstrates that collisions do not cause significant CO vibrational relaxation under the conditions of our measurements.

To investigate the possibility of collisional quenching of the excited electronic states N(^{2}D,^{2}P), LIF spectra were also recorded at different delay times between the photolysis and probe lasers and at different positions of the lasers in the expansion. As the collision rate and number density in the expanding jet fall off rapidly with distance from the source, the position of the photolysis laser in the expansion region determines the collision environment in which the excited atoms are formed. Number densities as a function of distance from the source were estimated using expressions given by Lubman et al.[25] and were averaged over the finite width (2 mm) of the photolysis laser beam. The laser delay between the formation of the atoms and their detection gives an estimate of the time frame for collisions to occur. At the shortest delay times and lowest densities used (4.1×10^{10} molec cm^{-3} s), the N(^{2}D)/N(^{2}P) intensity ratio was a factor of 3 smaller than that obtained at the longest delay times and highest densities (5.0×10^{13} molec cm^{-3} s).

It was not practical to extend the measurements to conditions of fewer collisions, because the scattered light from the 193-nm photolysis laser prevented reliable detection of the much weaker N(^{2}P) LIF signal. The N(^{2}D) LIF signal, however, was readily detected down to (density $\times$ delay) values of 8.1×10^9 molec cm^{-3} s. It was observed that the spectral line width progressively broadened as the (density $\times$ delay) product decreased. This trend was also seen for N(^{2}P) at somewhat higher (density $\times$ delay) conditions but was not as pronounced.

Although the photolysis wavelength of 193 nm is below threshold for production of O + CN(A$^2\Pi$), the additional internal energy of NCO is enough to reach the threshold of channel 5. We searched for the CN(A) state by LIF probing with the B$^2\Sigma^+ \leftarrow$ A$^2\Pi$ transition, but no fluorescence was detected.

Data Analysis. The vibrational distribution of the CO products was measured by monitoring the A$^1\Pi \leftarrow$ X$^1\Sigma^+$ band LIF intensity as the probe laser was scanned over the rotational structure of several vibronic transitions. CO vibrational bands were assigned by comparison with simulated spectra generated using the updated A$^1\Pi$ state constants of Field et al.[26] Good agreement of normalized experimental and simulated spectra was routinely achieved with adjustment of four parameters: rotational temperature (typically 15 K), VUV laser bandwidth (typically 0.21 cm^{-1}), a shift in the wavelength scale to account for a calibration error in the ω_2 dye laser, and an intensity scale factor. The relative vibrational population was extracted from integration of each simulated band. Integrated band intensities were converted to relative vibrational populations by dividing by the appropriate Franck−Condon factor.[27] Since the detection efficiency of the CO LIF was wavelength dependent, the band intensities were also corrected for the filter transmission and the photomultiplier quantum efficiency. These factors varied by nearly a factor of 2, depending on which upper level was excited in the CO A$^1\Pi \leftarrow$ X$^1\Sigma^+$ transition probed.

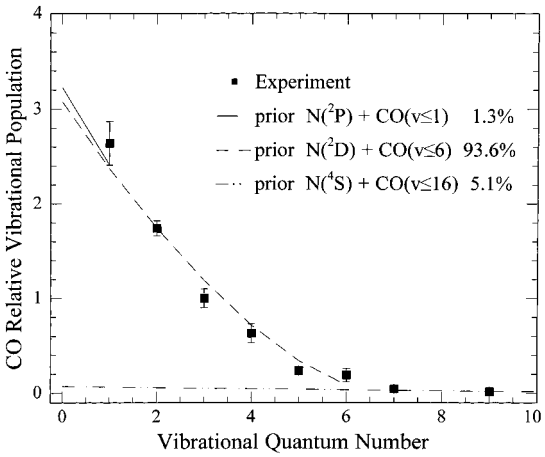

Figure 7. The observed CO vibrational distribution is compared with calculated prior distributions for the three channels producing N(^{4}S,^{2}D,^{2}P). The prior distributions have been scaled to agree with the observed distribution.

TABLE 1: Comparison of the Observed Distribution of CO Relative Vibrational Population with the Prediction of a Franck−Condon Model

v	relative population	Franck−Condon factor	v	relative population	Franck−Condon factor
0		0.313	5	0.235 ± 0.021	0.006
1	2.64 ± 0.23	0.357	6	0.19 ± 0.07	0.001
2	1.74 ± 0.08	0.212	7	0.045 ± 0.011	
3	1.0 ± 0.1	0.085	9	0.015 ± 0.005	
4	0.63 ± 0.10	0.025			

The CO vibrational distribution was pieced together from repeated scans over many segments of a wide wavelength interval (149−175 nm) and taken over several weeks. Relative populations within each day's accumulation of scans over several vibrational bands were determined by scaling to those scans probing a particular vibrational level, typically v''=3. In spectral regions where v',v'' = 3 bands were not present, other bands were taken as the reference and the resulting ratios later rescaled to v'' = 3. Good agreement was observed between relative populations obtained from scans that probed the same vibrational levels but with different bands in other spectral regions except for v'' = 0, which will be discussed below. The results for the CO vibrational state distribution are presented in Table 1 and Figure 7.

No reliable estimate of the CO(v=0) population could be obtained due to a large background of thermal (300 K) CO. This background made its presence known by absorption peaks in the VUV monitor signal. The absorption peaks varied in size on a daily basis, reaching as high as 90% of the total VUV monitor signal. The CO background persisted for days, even after continual pumping on the system at pressures of 10^{-7} Torr. Due to the long (80 cm) path length of the VUV laser radiation through the chamber to the monitor, it was not possible to determine the extent to which the VUV had been attenuated at the point of intersection with the jet. As a result, CO(v=0) LIF signals from the dissociation of NCO could not be properly normalized, as evidenced by large disagreements (factor of 3) in the CO(v=0)/CO(v=1) population ratios obtained by scanning different bands.

Atomic N* populations were determined from the integrated intensities of normalized spectra using oscillator strengths

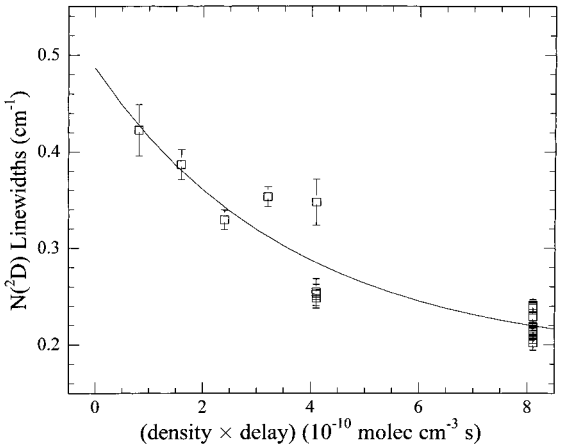

Figure 8. Translational relaxation of the N(^{2}D) Doppler line shape by collisions in the jet expansion region. The solid line was obtained by fitting an exponential decay function to the data.

derived from tabulated Einstein *A* coefficients for the 3s $^2P_J \leftarrow 2s^22p^3\ ^2D_J$ and 3s $^2P_J \leftarrow 2s^22p^3\ ^2P_J$ transitions.[23] Although the N(^{2}D) and N(^{2}P) transitions are well-separated in wavelength, the upper state 3s ^2P_J is common to both, and the strong emission is dominated by fluorescence back to the ^{2}D levels. The efficiency of the fluorescence detection system is thus nearly independent of the excitation wavelength, and the resulting emission correction factors differ by less than 5%. This is not the case, however, for the detection efficiency of the VUV monitor system, where the filter band-pass, the diffuser transmittance, and the quantum efficiency of the photomultiplier are all strongly wavelength dependent. We estimate from measured transmission curves and photocathode specifications that the VUV monitor is more sensitive by a factor of 5.4 to wavelengths near 149 nm (^{2}D) than to wavelengths near 175 nm (^{2}P). This factor was included in the normalization of the atomic spectra to the fluctuations of the VUV laser radiation.

For the N($^2P_J \leftarrow {}^2D_J$) system, the three allowed transitions are well-resolved and the relative intensities agree well with the 9:1:5 ratio expected for a statistical population of the two spin−orbit states $^2D_{3/2}$ and $^2D_{5/2}$ (see Figure 5). For the N($^2P_J \leftarrow {}^2P_J$) system, the four allowed transitions appear as two closely spaced doublets (see Figure 6). Again, the spectral intensities appear to agree well with the 1:5:2:1 ratio expected for a statistical population of the two spin−orbit states $^2P_{3/2}$ and $^2P_{1/2}$. The doublet spacing of the ground state (0.368 cm^{-1}) is well-resolved under conditions of translational relaxation and scans with small step size. The populations determined from the three spectral components detected for N(^{2}D) were consistent, as were the populations determined from the four N(^{2}P) lines.

A direct comparison of the N(^{2}D) and N(^{2}P) LIF intensities was obtained by using two sets of cuvettes, dye circulators, and dye solutions and alternately switching the pair in and out of the ω_2 dye laser in order to scan over the two wavelength regions of interest. The population ratio N($^2D_{3/2,\ 5/2}$)/N($^2P_{3/2,\ 1/2}$) was found to be dependent on the (density × delay) product and was determined to be 72 ± 18 at 4.1 × 10^{10} molec cm^{-3} s, 97 ± 13 at 8.1 × 10^{10} molec cm^{-3} s, and 250 ± 29 at 5.0 × 10^{13} molec cm^{-3} s.

The spectral line widths of both N(^{2}D) and N(^{2}P) were observed to increase as the (density × delay) product decreased. Widths of the spectral lines were obtained as full widths at half-maximum (fwhm) from the fit of Gaussian functions to the spectra and deconvoluted from the VUV laser bandwidth. An exponential decay function of the form ($y = a + be^{-x/c}$) was fitted to the deconvoluted line widths as a function of the (number density × laser delay) product for N(^{2}D). Extrapolating the line widths to zero (density × delay) or "zero collisions" is equivalent to the sum of the parameters from the fit $a + b$, and yields a fwhm of 0.487 ± 0.045 cm^{-1} for "nascent" N(^{2}D). The range parameter, *c*, in the exponential was determined to be (3.7 ± 1.4) × 10^{-10} cm^3 molec^{-1} s^{-1}. The data and fit are shown in Figure 8. The error bars represent the uncertainty in the width parameter obtained from Gaussian fits to the line shapes. Despite the broadening of the N(^{2}P) line shapes observed at low (density × delay) products, the effect was modest and the poor signal-to-noise ratio of the data did not allow an analysis similar to that for the N(^{2}D) line shapes. As a result, we report only a lower limit for the deconvoluted, "nascent" line width of 0.19 ± 0.01 cm^{-1} for N(^{2}P), obtained at a (density × delay) value of 4.1 × 10^{10} molec cm^{-3} s.

Discussion

The gas-phase reaction of CN with O_2 used to generate the NCO radicals in these experiments has three exothermic pathways that lead to products:

$$CN + O_2 \rightarrow NCO + O \quad \Delta H^0 = -29\ \text{kJ/mol} \qquad (11)$$

$$\rightarrow CO + NO \quad \Delta H^0 = -461\ \text{kJ/mol} \qquad (12)$$

$$\rightarrow N(^4S) + CO_2 \quad \Delta H^0 = -359\ \text{kJ/mol} \qquad (13)$$

The simple abstraction channel 11 is the dominant pathway, accounting for more than 70% of the reaction yield.[28] The relative importance of the most exothermic channel (12), however, is still under debate, as the results from several experimental determinations range from 6% to 29%.[28] The pathway 13, resulting in atomic nitrogen and carbon dioxide as coproducts, is a minor channel (2%)[29] but is sufficiently exothermic to access either N(^{2}D) or N(^{2}P). The results of the power dependence experiments presented in Figure 3 clearly show a quadratic dependence of the CO, N(^{2}D), and N(^{2}P) products on the 193-nm laser power. This rules out processes 12 and 13 as the sources of CO and N* in our experiments, as they would be characterized by a linear dependence on the 193-nm laser power.

Since the number densities of both radical and molecular species are high in the region of the expansion just downstream of the jet orifice where NCO is made, there is the possibility of secondary reactions giving rise to N* atoms and/or CO molecules. The following are examples of very fast reactions for which the N* and CO products would display a quadratic dependence on the 193-nm laser power:

$$NCO + O \rightarrow CO + NO \quad \Delta H^0 = -425\ \text{kJ/mol} \qquad (14)$$

$$CN + O \rightarrow N(^4S) + CO \quad \Delta H^0 = -326\ \text{kJ/mol} \qquad (15)$$

$$\rightarrow N(^2D) + CO \quad \Delta H^0 = -95\ \text{kJ/mol} \qquad (16)$$

Consideration of reactions 14−16 together with the C_2N_2 absorption step 8 and the fast CN + O_2 reaction 9 does reveal a differentiating feature from the proposed scheme 8−10, in which the N* and CO are produced by the 193-nm photolysis of NCO. The product signal from the secondary reactions will be quadratically dependent upon the fraction of C_2N_2 in the gas mixture, whereas the 193-nm photolysis of NCO scheme will be linear. In diagnostic studies, it was clearly demonstrated that the N(^{2}D) LIF signal exhibited a linear dependence on the fraction of C_2N_2 in the gas mixture for a range of C_2N_2 fractions

differing by a factor of 5. The linear dependence on $[C_2N_2]$ is a strong confirmation that the observed N(^{2}D) and CO do result from NCO photochemistry rather than from secondary reactions.

The appearance of the vibrational distribution itself is further evidence that the CO does not come from any of the processes 12, 15, or 16. The CO vibrational distribution from CN + O is bimodal with peaks at $v = 0$ and 9 and extending to $v = 12$, while that from CN + O_2 is a monotonically decreasing distribution extending from $v = 0$ to 4.[30] The CO distribution observed in this work also falls monotonically, but less rapidly, and it reaches to $v = 6$, with further population extending in a long tail to at least $v = 9$, but with no secondary maximum. This evidence taken together with the C_2N_2 pressure study and the power dependence studies of the NCO, CO, and N* signals confirms that the 193-nm photodissociation of NCO is indeed the process being observed.

The CO Vibrational Distribution. The CO vibrational distribution we observe was determined under expansion conditions in which the CO was detected some 50 nozzle diameters downstream from where the NCO was generated and dissociated at 193 nm. During the 36 μs flight time to the detection volume, extensive collisional cooling of the rotational and translational degrees of freedom occurred, resulting in 15 K rotational distributions for CN, CO, and NCO and laser bandwidth limited spectral line shapes. However, the vibrational degree of freedom appeared to be affected by collisions only in the case of the low-frequency NCO bending vibrations and not for the much higher stretching frequency of the diatomic product CO. This has been confirmed by energy transfer experiments in which the rate constants measured for vibrational relaxation of NCO bending vibrations with He or Ar are 4 orders of magnitude greater than are the corresponding rates of relaxation of CO(v=1) in collisions with He or O_2.[31−33]

Self-relaxation of vibrationally excited CO by collisions with CO(v=0) has been observed to be an efficient process,[34] with measured rate constants for relaxation of low vibrational levels of CO that are comparable to those obtained for NCO bending relaxation by Ar. For higher vibrational levels of CO, however, the relaxation rate constants decline by 3 orders of magnitude over the range from CO(v=3) to CO(v=14). In our experiments, the very much lower beam densities of CO(v) and CO(v=0), compared to NCO(ν_2) and Ar, result in insignificant self-relaxation of CO(v).

Diagnostic experiments were undertaken to determine the extent to which relaxation affected the CO vibrational distribution. Integrated CO LIF intensities for the (0,1) and the (4,4) bands were compared at several delays between production and detection, namely, 4, 8, and 36 μs. At each of these delays, the ratio of integrated intensities for the two vibrational bands was the same within the experimental uncertainties ($\pm 1\sigma$). Unfortunately, it was not possible to extend the diagnostic experiments to shorter delays, because of signal-to-noise limitations. Since most collisions occur early in the expansion (short delays), partial vibrational relaxation due to collisions in the first 4 μs of delay could not be ruled out.

Extensive vibrational excitation in CO was observed with population in levels up to $v = 9$. Dissociation in isoelectronic systems such as N_3 and N_2O^+ also reveal considerable internal energy in the respective N_2 and NO^+ fragments accompanying the N atoms.[35,36] Similar vibrational distributions to this work were inferred for the N_2 fragments in the N(^{4}S) and N(^{2}D) channels when N_3 was dissociated with approximately the same energies available to products as in this work. Both NCO and N_3 have elongated C−O (1.206 Å)[4] and N−N (1.18 Å)[37] bonds relative to the equilibrium bond lengths in free CO (1.128 Å) and N_2 (1.10 Å).[5] It is reasonable to expect that a sudden change in the bond length of the diatomic fragment upon dissociation will produce a distribution of vibrational states. A simple Franck−Condon model for the resulting vibrational distribution has been shown qualitatively to reproduce the N_2 vibrational distribution accompanying N(^{2}D) for the major channel in the N_3 dissociation.[35] A similar calculation for the NCO dissociation using Morse potential wave functions[38] predicts a CO vibrational distribution that peaks at $v = 1$ and has significant population out to $v = 4$. The results are compared with the experimentally observed distribution in Table 1.

The CO vibrational distribution has contributions from the three channels that differ in the electronic state of the atomic nitrogen coproduct. Because of the substantial energy spacings between the N(^{4}S,^{2}D,^{2}P) electronic levels, the thermodynamic limits to the vibrational levels in the CO coproduct from each channel are also substantially different. Ground-state atomic nitrogen (^{4}S) may accompany CO in vibrational levels up to $v = 16$, whereas for the excited states, N(^{2}D) and N(^{2}P), the limits on CO vibration are $v = 6$ and $v = 1$, respectively. Vibrationally excited CO with more than six quanta may then reasonably be attributed to the spin-forbidden channel, leading to ground-state N atoms. For CO with zero to six quanta of vibrational energy, there is an additional contribution from the spin-allowed channel leading to N(^{2}D). For CO with up to one quanta of vibrational energy, there is a third contribution from another spin-allowed channel leading to N(^{2}P). The vibrational distribution displayed in Figure 7 and listed in Table 1 clearly shows demarcation between two of the regions of population: a low population tail above $v = 6$ and a significant rise in population below $v = 6$. There is not such an obvious difference in the low ($v = 0-1$) region, where the N(^{2}P) channel contributes, due in part to the lack of a reliable estimate of the CO(v=0) relative population. However, the population of CO in $v = 1$ does not appear to be very different from what might be expected from extrapolating the trend toward increasing population at low v. This would indicate a minor contribution from the N(^{2}P) producing channel.

The correspondence of the CO vibrational distribution with the thermodynamic limits of the three channels of NCO photolysis suggests that the branching ratio between the channels may be determined from the CO vibrational distribution. Such an interpretation has been employed to determine the branching ratio in the case of the CN + O reaction channels 15 and 16.[30] There the CO vibrational distribution was observed to be bimodal with widely separated peaks at $v = 0$ and $v = 9$ and a distinct valley at $v = 6$. A branching ratio of 4:1 was determined in favor of the N(^{2}D) channel, which peaked at the lower vibrational levels. A trajectory calculation on a LEPS surface showed that the CO distribution from the N(^{4}S) channel did not contribute to the CO distribution from the N(^{2}D) channel for CO vibrational levels $v < 7$.

The deconvolution of the three channels in the photolysis of NCO at 193 nm is somewhat less straightforward, because there is overlap between the contributions to the CO vibrational distribution. Consequently, we generated a model CO vibrational distribution for each channel by using the prior distribution that is based on maximum entropy considerations and the conservation of energy:[39]

$$P(v) \propto \{1 - f_v\}^{3/2}$$

where

$$f_v = E(\mathrm{CO}(v))/[h\nu - D_0(\mathrm{N{-}CO}) - E(\mathrm{N^*})]$$

The denominator in f_v is the available energy after taking into account the photon energy (193 nm), the bond dissociation energy (2.38 eV),[18] and the electronic energy of the N atom. The resulting prior distribution for CO from the channel leading to ground state N atoms was scaled to match the experimental distribution at $v = 7$ and 9, where only that channel contributes. The prior distribution for CO from the N(^{2}D) channel was then scaled to make up the difference between the CO contribution from the N(^{4}S) channel and the experimental distribution at $v = 2-6$. The difference between the experimental distribution and the scaled up contributions from the N(^{4}S) and N(^{2}D) channels at $v = 1$ was attributed to the CO contribution from the N(^{2}P) channel. The resulting CO prior distributions for the N(^{4}S) channel, for the sum of the N(^{4}S) and N(^{2}D) channels, and for the sum of all three channels are displayed in Figure 7 along with the experimental distribution.

The agreement of this simple model with experiment is only partially satisfactory, because without data for CO in $v = 0$ and for higher vibrational levels in the range $v = 10-16$, the comparison with the model is incomplete. The lack of data for CO(v=0) leaves only the vibrational population in $v = 1$ to determine the scale factor for the prior distribution of the N(^{2}P) channel. The difference between the experimentally derived ($v = 1$) population and the sum of the contributions from the scaled prior distributions for the N(^{2}D,^{4}S) channels is on the order of the experimental uncertainty. Thus, the scale factor for the N(^{2}P) prior distribution ranges from 0.15 to 1.9; results in an N(^{2}D):N(^{2}P) branching ratio between 50 and 4, respectively; and predicts the relative population for CO(v=0) to be from 3.2 to 5.0. The high end of the range of the N(^{2}D):N(^{2}P) branching ratio is reasonably close to the value of 72 ± 18 measured directly at the lowest (density × delay) conditions. The N(^{2}D):N(^{4}S) branching ratio was not affected by the choice of the scale factor for the N(^{2}P) channel, since it was calculated from scaling the prior distributions to match the data for $v = 2-7$, 9. The resulting N(^{2}D):N(^{4}S) branching ratio was 18.5 ± 6.7.

It must be pointed out that the prior distributions were calculated by assuming that the internal energy of NCO was negligible. Bulb experiments investigating the vibronic energy disposal in the NCO ($\tilde{X}$) product from the reaction of CN + O_2, however, have shown the bending motion of NCO to be highly excited.[40,41] Sauder et al.[40] observed 80 different vibronic levels in the NCO ground electronic state with energies up to 51.5 kJ mol^{-1}. They estimated average vibronic energies to be 12.7 ± 2.1 kJ mol^{-1} in the bending motion and 5 kJ mol^{-1} in the symmetric stretch. In our work, with NCO produced and photolyzed within the 20 ns pulse duration of the 193-nm laser, the number of collisions with Ar or C_2N_2 or O_2 in the jet expansion is insufficient to significantly relax the vibronic excitation before dissociation.[16,31,40,42] It is not clear, however, that the entire NCO internal energy needs to be considered as available energy for disposal into CO vibration. The largely bending excitation in the NCO will most likely be transferred to rotational motion of the CO fragment, and the effect of the remaining NCO stretching vibrational energy when included in the calculation of the prior distribution is negligible. If, however, both NCO bending and stretching vibrations are included, the range of CO vibrational levels accessible to each channel increases by one quantum and the model N(^{2}D):N(^{2}P) branching ratio disagrees substantially with the experimental result. The N(^{2}D): N(^{4}S) branching ratio, on the other hand, is unaffected by the extra available energy, as it is a small fraction of the total for this channel.

We have used this simple model of the prior distribution as a means of separating out the contributions of the three channels to the CO distribution. If the CO vibrational distribution was partially relaxed, then the population in the high vibrational levels would be underestimated and the inferred N atom branching ratios would underestimate N(^{4}S) and possibly N(^{2}D) relative to N(^{2}P). For reasonable assumptions about the available energy for the N(^{2}P) channel, however, the modeled contributions of the N(^{2}D) and N(^{2}P) channels to the CO vibrational distribution are in fair agreement with our independent experimental determination of the N(^{2}D):N(^{2}P) branching ratio, indicating that vibrational relaxation is not a serious problem. The model provides the only estimate of the relative contributions to the CO vibrational distribution from the N(^{4}S) and N(^{2}D) channels. The resulting branching ratio appears to be insensitive to details about the internal energy assigned to the NCO parent in the model calculations. Combination of the model N(^{4}S):N(^{2}D) result with the experimental N(^{2}D):N(^{2}P) determination, yields an overall branching ratio of N(^{4}S):N(^{2}D):N(^{2}P) of (5.1 ± 1.8):(93.6 ± 4.8):(1.3 ± 0.3). The error estimates ($\pm 1\sigma$) for N(^{4}S) and N(^{2}D) reflect the uncertainties in the scale factors determined in the comparison of the prior distributions with the observed CO vibrational distribution. The error estimate for N(^{2}P) is derived from the direct determination of the N(^{2}D):N(^{2}P) branching ratio and by attributing all of the uncertainty to the much weaker N(^{2}P) signal. Using the prior distributions for the two lower energy channels, the average energy disposals in CO vibration are calculated to be 8870 and 3140 cm^{-1} for the N(^{4}S) and N(^{2}D) channels. These values correspond to fractions of the available energy appearing in product CO vibration of 27% and 24%, respectively.

N(^{2}D):N(^{2}P) Branching Ratio. This is the first report of the direct detection of electronically excited nitrogen atoms (^{2}D, ^{2}P) from the photodissociation of NCO at 193 nm. Previous workers using microwave discharge resonance lamps to excite similar atomic transitions were unable to detect the N* products.[20] Although both experiments used a 193-nm pulsed laser for photolysis, the high intensity and the short pulse duration of the VUV probe laser used here provide a greater detection sensitivity than the CW fluorescence lamps used in that work.

We measured the N(^{2}D):N(^{2}P) branching ratio by directly comparing the intensities of consecutive scans over the N(^{2}D) and the N(^{2}P) transitions. Between scans it was necessary to switch cuvettes and dye solutions in one of the dye lasers involved in the VUV generation scheme, because these transitions are in different spectral regions. Normalization to the VUV probe laser pulse energies required a correction factor of 5.4, since the VUV monitor was not equally sensitive in the two wavelength regions. This factor was calculated from filter transmission curves and specifications for the photomultiplier quantum yield. In light of the fairly large correction factor, we also measured the N(^{2}D):N(^{2}P) branching ratio using an indirect method that compared LIF intensities from N* transitions and CO (A−X) vibrational bands. Because the N* and CO LIF signals were obtained in the same wavelength region, no correction for the wavelength dependence of the detector efficiency was required for the N*:CO(v) ratio. In this way, N(^{2}D) was compared to CO (v=1) and N(^{2}P) was compared to CO(v=5) (see Figures 5 and 6). The transitions probing both N(^{2}P) and N(^{2}D) share a common upper state, so that the detection efficiency of the resulting fluorescence was the same for both. The excited CO bands, on the other hand, fluoresced from different upper states, so that it was necessary to correct

the relative vibrational populations for filter transmissions and photomultiplier quantum yields. In the case of the CO(3,1) and (2,5) bands used here, the correction factors differed only by about 5%. The resulting branching ratios were obtained: $N(^2D)$:$CO(v=1) = 5.01 \pm 0.22$, $N(^2P)$:$CO(v=5) = 0.268 \pm 0.047$, and $CO(v=1)$:$CO(v=5) = 11.23 \pm 1.01$. These three ratios combined give a $N(^2D)$:$N(^2P)$ branching ratio of 210 ± 42 at a (density × delay) product on the order of 10^{13} molec cm^{-3} s. This value agrees well with the direct determination of 250 ± 29 at a (density × delay) product of 5.0×10^{13} molec cm^{-3} s. The consistency of the results from the two methods lends credence to the direct method and the use of the substantial correction factor for normalization to the VUV laser energies. The comparison was only possible, however, at the larger (density × delay) products, where the CO rotational distributions were cooled in the expansion. The resulting intense and narrow distributions could thus be scanned quickly with a sufficiently high signal-to-noise ratio in order to compare with the N* intensity.

Since it was observed that the $N(^2D)$:$N(^2P)$ branching ratio increased with the (density × delay) product, there must be one or more selective loss processes occurring. Selective and significant loss of fast N* atoms by escape from the expansion region prior to detection is unlikely at the atomic velocities allowed by the available energy. Experiments in our lab with much faster $O(^3P)$ atoms (5000 ms^{-1}) generated in the photolysis of ozone at 266 nm indicate that the fast atoms are quickly entrained in the beam.[43] Selective loss by reaction or quenching would most probably involve collisions with the C_2N_2, O_2, and Ar components of the gas mixture. Electronic quenching collisions with Ar are very inefficient; the measured rate constants are on the order of 10^{-16} cm^3 molec^{-1} s^{-1} near 300 K.[44,45] Much more efficient quenching of $N(^2D)$ and $N(^4S)$ by C_2N_2 has been observed with rate constants of $\sim 10^{-11}$ cm^{-3} molec^{-1} s^{-1} at 298 K, but no information is available for $N(^2P)$.[46,47] Loss of N* by reaction with O_2 has been more fully studied, and temperature dependent rate constant expressions have been recently evaluated; the recommended rate constants are 9.7×10^{-12} e$^{-185/T}$ and 3.1×10^{-12} e$^{-60/T}$ cm^{-3} molec^{-1} s^{-1} for $N(^2D)$ and $N(^2P)$, respectively.[48] It is clear that at the highest conditions of (density × delay) used in our experiments, quenching with C_2N_2 or reaction with O_2 are significant processes. While we do not fully understand the selective nature, it may be that the cooling in the expansion favors reaction or quenching of $N(^2P)$. Fortunately, at the experimental conditions of lowest (density × delay), however, these processes are 1−2 orders of magnitude slower and do not affect the measured branching ratio.

Branching in the production of $N(^2D,^2P)$ has also been observed in the dissociations of the isoelectronic systems of N_3 and N_2O^+. For N_3 dissociation in the ($\tilde{B}^2\Sigma^+$) state at energies about 1 eV above the $N(^2P)$ channel threshold, the major channel produces $N(^2D)$ as in the dissociation of NCO. However, the $N(^2D)$:$N(^2P)$ ratio of 5 is much less than for NCO.[35] The dissociation of N_2O^+ in the ($\tilde{B}^2\Pi$) state also results in a much lower $N(^2D)$:$N(^2P)$ ratio. Similar to the NCO dissociation at an energy just above the $N(^2P)$ threshold, $N(^2D)$ is the favored channel but only by a factor of 2.4 in the case of N_2O^+ compared to 72 in the NCO case.[49] At higher energies, however, $N(^2P)$ becomes the major channel, and upon excitation to the N_2O^+ $\tilde{C}$ state, the $N(^2D)$ channel closes, leaving $N(^2P)$ as the sole coproduct with NO^+.[36]

Average Energy Disposal in the $N(^2D)$ + CO Channel. The spectral widths (fwhm) of the N* lines were observed to broaden at the lowest (density × laser delay) conditions. This was more apparent with the $N(^2D)$ transitions, since the stronger LIF signals could be seen above the level of the scattered 193-nm laser light down to laser delays as low as 100 ns. The widths displayed an exponential decay with laser delay over the range of 0.1−1.0 μs. Because the probe and photolysis lasers were spatially overlapped, the series of measurements probed the same region of density in the jet, so that the (density × laser delay) values genuinely reflect the kinetics of the process of translational relaxation. The VUV probe laser bandwidth was deconvoluted from the experimental line shapes, and an exponential decay parameter of $(3.7 \pm 1.4) \times 10^{-10}$ cm^3 molec^{-1} s^{-1} was obtained from the fit to the plot of spectral widths vs (density × delay). This value is essentially a gas kinetic rate constant for the deactivation of translational energy of $N(^2D)$ by collisions with Ar, although collisions with O_2 and C_2N_2 also likely contribute to the process. The Doppler width of the transition reflecting "zero" collisions was obtained from the fitting parameters as 0.487 ± 0.045 cm^{-1}. Due to the weaker $N(^2P)$ signal, only a lower limit on the nascent Doppler width could be obtained as 0.19 ± 0.01 cm^{-1} at the (density × delay) value of 8.1×10^{-10} molec cm^{-3} s.

An average $N(^2D)$ velocity of 1090 ± 101 ms^{-1} was obtained from the estimate of the "zero-collision" Doppler width. Assuming that the decay rate constant obtained from the fit may be approximated as the product of the $N(^2D)$ velocity and the cross section for translational relaxation of $N(^2D)$ by collisions with Ar, a cross section of 34 Å^2 is obtained. Similar cross sections in the range 20−40 Å^2 have been observed in bulb experiments for the translational relaxation of fast $S(^1D)$ with Ar.[50] With the consistency of the average $N(^2D)$ velocity and decay rate constant from the line width experiments thus confirmed, the average translational energy in the nascent $N(^2D)$ + CO channel may be estimated as 1040 ± 190 cm^{-1}. This corresponds to an average fraction of (7.8 ± 1.3)% of the available energy appearing in translation. Having accounted for the average energy in vibration (24%) and translation (8%), the remainder (68%) of the available energy must therefore appear in the rotation of the CO fragment. This amounts to 9050 cm^{-1} as the average CO rotational energy for this channel. In these estimates of the average product energy partitioning, both the effect of relaxation of the CO vibrational distribution and the contribution of the parent NCO internal excitation to the available energy were neglected. Fortuitously, these effects tend to cancel because the largely bending excitation in NCO should be converted to CO rotation upon dissociation, while correction for vibrational relaxation results in a decreased fraction of energy ending up in CO rotation.

This very large disposal of energy into CO rotation is much greater than the contributions from parent ground-state NCO bending and rotational excitation generated in the photoinitiated reaction CN + O_2. Simple classical models show that at most only 15% of the CO rotational energy may be due to parent NCO internal motion.[51] Similarly, models of impulsive type dissociations do not predict the extensive rotational excitation and the low translational energy release observed here.[51] It is much more likely that the rotational excitation arises from dissociation through an excited state with a bent N−CO geometry, where the excited potential energy surface exerts a strong torque on the departing CO.

NCO Excited States Accessible at 193 nm. Both N_2O^+ and NCO are linear and asymmetric triatomic species. More importantly, they are also isoelectronic. The energetics and dissociation of the N_2O^+ system, however, have been studied

much more extensively than NCO. Photoelectron spectroscopy of N_2O^+, for example, has clearly demonstrated the existence of the four lowest energy bound electronic states: $\tilde{X}(^2\Pi)$, $\tilde{A}(^2\Sigma^+)$, $\tilde{B}(^2\Pi)$, and $\tilde{C}(^2\Sigma^+)$.[36] Recent ab initio theoretical calculations have predicted these and higher energy bound and dissociative states.[15] The corresponding NCO ($\tilde{X}$, $\tilde{A}$, and $\tilde{B}$) states have been observed experimentally, but there have been few theoretical investigations of these or the higher energy electronic states.[12,14,16,19] A fairly low level molecular orbital calculation dating back to 1975 predicts transition energies and oscillator strengths for excitation to eight electronic states of NCO.[14] The resulting NCO transition energies calculated for the Franck−Condon region agree well with experimental results for the $\tilde{A}$ and $\tilde{B}$ states. The strongest absorption to the $\tilde{A}$ state is the origin band,[40] while the predicted excitation to the $\tilde{B}$ state reaches vibrationally excited levels known to be near the peak in the photodissociation cross section.[18] A comparison of the NCO electronic energies and those of N_2O^+ from these two disparate calculations shows that the vertical transition energies to the NCO ($\tilde{A}$, $\tilde{B}$, $\tilde{C}$ and $\tilde{D}$) states are consistently about 1 eV (0.80, 1.02, 1.27, 1.04) lower than the corresponding values for N_2O^+.[14,18] Both the $\tilde{C}(^2\Sigma^+)$ and the $\tilde{D}(^2\Pi)$ states of NCO are predicted to have appreciable oscillator strength for transitions from the ground state at 50 900 and 47 700 cm^{-1}, respectively, and are likely to be accessible at the excitation wavelength of 193.3 nm (51 733 cm^{-1}).

There has been some experimental evidence of one or more NCO states in the spectral region accessed by 193-nm excitation. Liu and Coombe[20] resolved fluorescence from an unknown state after excitation of NCO at 193.3 nm. The wavelength spacing between the bands corresponded to the energy spacing between low vibrational levels of the $\tilde{A}$ state. They concluded that the unknown state was linear after noting that the resolved fluorescence terminated only on stretching vibrational levels. They also inferred the presence of a bent excited state of NCO from the bimodal appearance of the observed CN product rotational distributions.

Whatever the identity of the state or states initially excited at 193 nm, it is clear that there must be more than one mechanism of dissociation and more than one NCO excited state involved. The observation of all four product channels (1−4) with their associated correlations with different NCO states makes this a necessity. Also, by analogy with the N_2O^+ system, it is unlikely that the $\tilde{C}$ and $\tilde{D}$ states of NCO correlate directly with any of the four product channels but are influenced by surface crossings and nonadiabatic interactions. These have already been shown to be of importance in the spin-forbidden channel at low excitation energies near the $\tilde{B}$ state origin.[19]

Conclusions

NCO($\tilde{X}$) was produced and dissociated at 193 nm by a two-photon process early in the jet expansion of a $C_2N_2/O_2/Ar$ gas mixture. The first photon dissociated C_2N_2 to produce CN radicals that then reacted sufficiently with O_2 to produce detectable amounts of NCO. Within the same laser pulse of 20 ns duration, the NCO absorbed a second 193-nm photon and dissociated to CO and $N(^2P,^2D,^4S)$. Excited states of atomic nitrogen (^2P, ^2D) were directly detected by VUV LIF, and an upper bound on the $N(^2D)/N(^2P)$ branching ratio was determined to be 72 ± 18. Selective loss of $N(^2P)$ was observed at points later in the expansion, as characterized by branching ratios as high as 250 ± 29.

The CO vibrational distribution contained contributions from the three channels producing atomic nitrogen but was dominated by the channel producing $N(^2D)$ as coproduct with CO(v=0−6). Higher vibrational levels were assigned to the channel that produced ground-state atomic $N(^4S)$. The contributions from these two channels were well-reproduced by a model in which the separate channels were represented with prior distributions scaled in the ratio $N(^2D)/N(^4S)$ of 18.5 ± 6.7. The combined $N(^4S):N(^2D):N(^2P)$ branching ratio that incorporates the direct measurement of $N(^2D)$ and $N(^2P)$ and the prior model results is thus (5.1 ± 1.8):(93.6 ± 4.8):(1.3 ± 0.3).

The average energy disposal in the dominant $N(^2D)$ + CO channel was determined to be 8% into relative translation and 24% into CO vibration. The remaining 68% of the available energy is expected to appear in CO rotation, suggesting that the dissociation of the excited state of NCO must pass through a bent geometry.

Acknowledgment. We thank Prof. Paul J. Dagdigian for making his NCO simulation programs available to us. We also thank Prof. J. H. D. Eland for providing us with details of his work on the dissociation of N_2O^+ (ref 36). This research was supported by the National Science Foundation under grant CHE-9901065.

References and Notes

(1) Holland, R.; Style, D. W. G.; Dixon, R. N.; Ramsay, D. A. *Nature* **1958**, *182*, 337.
(2) Dixon, R. N. *Can. J. Phys.* **1960**, *38*, 10−16.
(3) Dixon, R. N. *Philos. Trans. R. Soc. London A* **1960**, *252*, 165.
(4) Misra, P.; Mathews, C. W.; Ramsay, D. A. *J. Mol. Spectrosc.* **1988**, *130*, 419−23.
(5) Herzberg, G. *Molecular Spectra and Molecular Structure: I. Spectra of Diatomic Molecules*, 2nd ed.; Van Nostrand Reinhold: New York, 1950.
(6) Winnewisser, G.; Maki, A. G.; Johnson, D. R. *J. Mol. Spectroscopy* **1971**, *39*, 149.
(7) Miller, J. A.; Branch, M. C.; McLean, W. J.; Chandler, D. W.; Smooke, M. D.; Kee, R. J. *Twentieth Symposium (International) on Combustion* **1984**, 673−684.
(8) Debrou, G. B.; Goodings, J. M.; Bohme, D. K. *Combust. Flame* **1980**, *39*, 1−19.
(9) Haynes, B. S. *Combust. Flame* **1977**, *28*, 113-21.
(10) Miller, J. A.; Bowman, C. T. *Int. J. Chem. Kinet.* **1991**, *23*, 289−313.
(11) Siebers, D. L.; Caton, J. A. *Combust. Flame* **1990**, *79*, 31−46.
(12) Minaev, B. F.; Ivanova, N. M.; Muldahmetov, Z. M. *Spectrosc. Lett.* **1989**, *22*, 901−23.
(13) Callomon, J. H.; Creutzberg, F. *Philos. Trans. R. Soc. London, Ser. A* **1974**, *277*, 157−189.
(14) Carsky, P.; Kuhn, J.; Zahradnik, R. *J. Mol. Spectrosc.* **1975**, *55*, 120−30.
(15) Chambaud, G.; Gritli, H.; Rosmus, P.; Werner, H. J.; Knowles, P. J. *Mol. Phys.* **2000**, *98*, 1793−1802.
(16) Yao, J. L.; Fernandez, J. A.; Bernstein, E. R. *J. Chem. Phys.* **1997**, *107*, 8813−8822.
(17) Wright, S. A.; Dagdigian, P. J. *J. Chem. Phys.* **1996**, *104*, 8279−8291.
(18) Cyr, D. R.; Continetti, R. E.; Metz, R. B.; Osborn, D. L.; Neumark, D. M. *J. Chem. Phys.* **1992**, *97*, 4937−47.
(19) Alexander, M. H.; Werner, H.-J. unpublished work, discussed in refs 16−18.
(20) Liu, X.; Coombe, R. D. *J. Chem. Phys.* **1989**, *91*, 7543−9.
(21) Schoennenbeck, G.; Stuhl, F. *Chem. Phys. Lett.* **1997**, *264*, 199−204.
(22) Dobeck, L. M.; Lambert, H. M.; Kong, W.; Pisano, P. J.; Houston, P. L. *J. Phys. Chem. A* **1999**, *103*, 10312−10323.
(23) NIST Atomic Spectra Database; Version 2.0; NIST Standard Reference Database #78; http://physics.nist.gov/cgi-bin/AtData/main_asd.
(24) Hepburn, J. W. Generation of Coherent Vacuum Ultraviolet Radiation: Applications to High-Resolution Photoionization and Photoelectron Spectroscopy. In *Laser Techniques in Chemistry*; Myers, A. B., Rizzo, T. R., Eds.; Wiley-Interscience: New York, 1995; pp 149−183.
(25) Lubman, D. M.; Rettner, C. T.; Zare, R. N. *J. Phys. Chem.* **1982**, *86*, 1129−35.
(26) Field, R. W.; Wicke, B. G.; Simmons, J. D.; Tilford, S. G. *J. Mol. Spectrosc.* **1972**, *44*, 383−99.

(27) Waller, I. M.; Hepburn, J. W. *J. Chem. Phys.* **1988**, *88*, 6658−69. Note that the FCF values in their Table 2 for the (4,2), (5,2) and (7,4) bands are too large by a factor of 10.
(28) Smith, I. W. M. *Adv. Ser. Phys. Chem.* **1995**, *6*, 214−249.
(29) Rim, K. T.; Hershberger, J. F. *J. Phys. Chem. A* **1999**, *103*, 3721−25.
(30) Schmatjko, K. J.; Wolfrum, J. *Ber. Bunsen-Ges. Phys. Chem.* **1978**, *82*, 419−28.
(31) Astbury, C. J.; Hancock, G.; McKendrick, K. G. *J. Chem. Soc., Faraday Trans.* **1993**, *89*, 405−10.
(32) Wickham-Jones, C. T.; Williams, H. T.; Simpson, C. J. S. M. *J. Chem. Phys.* **1987**, *87*, 5294−301.
(33) Andrew, J. J.; McDermott, D. C.; Mills, S. P.; Simpson, C. J. S. M. *Chem. Phys.* **1991**, *153*, 247−58.
(34) DeLeon, R. L.; Rich, J. W. *Chem. Phys.* **1986**, *107*, 283−292.
(35) Continetti, R. E.; Cyr, D. R.; Osborn, D. L.; Leahy, D. J.; Neumark, D. M. *J. Chem. Phys.* **1993**, *99*, 2616−2631.
(36) Kinmond, E.; Eland, J. H. D.; Karlsson, L. *Int. J. Mass Spectrom.* **1999**, *185*, 437−447.
(37) Douglas, A. E.; Jones, W. J. *Can. J. Phys.* **1965**, *43*, 2216.
(38) Morse, P. M. *Phys. Rev.* **1929**, *34*, 57.
(39) Levine, R. D.; Bernstein, R. B. *Molecular Reaction Dynamics and Chemical Reactivity*; Oxford University Press: Toronto, 1987.
(40) Sauder, D. G.; Patel-Misra, D.; Dagdigian, P. J. *J. Chem. Phys.* **1991**, *95*, 1696−707.
(41) Phillips, L. F.; Smith, I. W. M.; Tuckett, R. P.; Whitham, C. J. *Chem. Phys. Lett.* **1991**, *183*, 254−63.
(42) Macdonald, R. G.; Liu, K.; Sonnenfroh, D. M.; Liu, D. J. *Can. J. Chem.* **1994**, *72*, 660−72.
(43) Pisano, P. J.; Westley, M. S.; Houston, P. L. *Chem. Phys. Lett.* **2000**, *318*, 385−392.
(44) Lin, C.-L.; Kaufman, F. *J. Chem. Phys.* **1971**, *55*, 3760−70.
(45) Iannuzzi, M. P.; Kaufman, F. *J. Chem. Phys.* **1980**, *73*, 4701−2.
(46) Safrany, D. R.; Jaster, W. *J. Phys. Chem.* **1968**, *72*, 3305−18.
(47) Black, G.; Jusinski, L. E.; Slanger, T. G. *Chem. Phys. Lett.* **1987**, *141*, 58−60.
(48) Herron, J. T. *J. Phys. Chem. Ref. Data* **1999**, *28*, 1453.
(49) Brehm, B.; Frey, R.; Kuestler, A.; Eland, J. H. D. *Int. J. Mass Spectrom. Ion Phys.* **1974**, *13*, 251−60.
(50) Nan, G.; Houston, P. L. *J. Chem. Phys.* **1992**, *97*, 7865−72.
(51) Fisher, W. H.; Carrington, T.; Filseth, S. V.; Sadowski, C. M.; Dugan, C. H. *Chem. Phys.* **1983**, *82*, 443−57.